Quasiparticle description of transition metal dichalcogenide nanoribbons

Wiliam Ferreira da Cunha,[1,*] Pedro Henrique de Oliveira Neto,[1] Luiz Antonio Ribeiro Junior,[1,2] and Geraldo Magela e Silva[1]
[1]*Institute of Physics, University of Brasilia, 70.919-970 Brasilia, Brazil*
[2]*Department of Physics, Chemistry and Biology, Linköping University, SE-58183 Linköping, Sweden*

(Received 30 July 2018; revised manuscript received 5 November 2018; published 2 January 2019)

An effective two-dimensional real-space model is developed to investigate the nature of charge distribution in nanoribbons of transition metal dichalcogenides. Our description is based on a lattice relaxation endowed tight-binding Hamiltonian with spin-orbit and Hubbard interactions, which is parameterized to describe molybdenum disulfide lattices. As our main finding, we observed that electron-phonon coupling induces the creation of quasiparticles such as polarons in the same fashion as observed in conducting polymers and graphene nanoribbons. These similarities suggest that the charge transport in transition metal dichalcogenides can also be mediated by quasiparticles, which is a fundamental aspect concerning the application of these structures in electronics. We determine a range of possible electron-phonon coupling that correctly describes the system and also the critical value where quasiparticle transport is present. Our findings may have profound consequences on the understanding of the transport mechanism of transition metal dichalcogenides nanoribbons.

DOI: 10.1103/PhysRevB.99.035405

One of the major challenges for contemporary optoelectronic technology concerns the choice of semiconducting materials suitable for developing new high-performance devices. A performance enhancement in the current state of the art for these devices has been achieved by replacing conventional semiconductor materials, such as silicon, with graphene [1]. However, its lack of a band gap can be a drawback, mostly when it comes to low-power electronics [2]. Alternatively, transition metal dichalcogenides (TMDCs), such as molybdenum disulfide (MoS_2), a semiconducting 2D material with sizable band gaps (around 1.8 and 1.3 eV for monolayer and bulk MOS_2 structures, respectively [3]), are promising candidates for overcoming this problem. TMDCs not only present a remarkable variety of possible applications, particularly regarding optoelectronics, but they also present interesting mechanical, chemical, and thermal properties [4,5]. Because TMDCs are promising materials for application in nanoelectronics and nanophotonics, the investigation of charge transport and optical properties in these materials is of particular importance.

Many works have been devoted to the understanding of the electrical behavior of TMDCs [6]. Conductivity regimes ranging from metallic to semiconducting are observed to depend on the nature of the system as well as on external conditions under which they are subjected [7]. Also, behaviors as distinct as charge density waves and superconductivity states have been reported in these materials [8–10]. In the light of such a wide span of different phenomena, the main question that arises concerns the most fundamental aspect of the electronic transport, namely, the nature of the charge carriers in these materials. By understanding the nature of the transport, the transition between the different transport regimes can be described and eventually explored. In this sense, although the literature is prolific when it comes to reporting useful effects of the charge transport, a comprehensive description of the kind of species responsible for the transport has not been carried out to date. By studying the properties of such species, a deeper understanding of their effect can be achieved. Although this kind of effort was recently carried out for different excitations in TMDCs [11–13], the electronic transport and the relation between charge and the lattice degrees of freedom still require a more complete description.

Aspects regarding electric and optical properties are deeply connected to both band structure and lattice properties of the systems. This is because in this kind of solid-state system the electronic and lattice degrees of freedom are strongly coupled in a way similar to how they are in organic semiconducting nanosystems [14–17]. Taking this analogy between organic semiconductors and TMDCs one step further would inevitably make one wonder whether quasiparticles such as polarons are present in the latter case, as they are in the former. More importantly, in terms of the physical parameters that describe the systems, we should understand what the conditions are for such a transport regime to arise. This is the specific question tackled by the present paper. Here, we propose an effective two-dimensional tight-binding model with lattice relaxation, spin-orbit coupling, and Hubbard interactions in order to describe the transport regime in monolayer nanoribbons of TMDCs. A careful choice of parameters allows us to describe MoS_2 as the trial species, so that our results can be compared to experimental ones. Nevertheless, it should be stressed that our model is suitable for different species of the class.

Our approach is inspired by previous modification, carried out by our own group [18,19], of the Su-Schrieffer-Heeger (SSH) Hamiltonian [20,21] to investigate charge dynamics in armchair graphene nanoribbons (AGNRs) [22,23]. In that study, we conceived a two-dimensional version of the SSH Hamiltonian with the inclusion of electric field. Even though the hexagonal symmetry and the almost flat geometry

*wiliam@unb.br

 ©2019 American Physical Society

that transition metal dichalcogenides nanoribbons (TMDCNs) present makes them reasonably similar to AGNRs, important additional modifications ought to be considered. First, we have to note that, unlike AGNRs, TMDCNs' unit cells contain two different species: transition metals and chalcogens. We therefore have to describe the model with two different sublattices. Second, as half of the atoms are metals with heavily loaded electronic clouds, Coulomb interactions are expected to be important. For this reason, we considered on-site and next-neighbor-site electron interactions by means of the inclusion of an extended Hubbard model. Third, because transition metals are heavy species, spin-orbit effects are known to be important to the correct description of the system [24]. Finally, TMDCNs are not exactly flat as AGNRs are. The relative displacement, however, is negligible when compared to the other dimensions of the system and can be effectively considered by a suitable parametrization of the model, specifically when choosing the desired electron-phonon coupling. It should be noted that with this modeling we focus our investigation on isolated and pristine lattices to obtain a general trend for the underlying quasiparticle properties in TMDCs. In this perspective, the use of anharmonic oscillator terms or the quantum-mechanical treatment of phonons is beyond the scope of the present work, which intends to present a clear interpretation of the physics in terms of the simplest Hamiltonian describing the system.

A detailed description of the calculations and methodology can be found in Appendix A. We describe the model Hamiltonian as $H = H_{tb} + H_{\text{latt1}} + H_{\text{latt2}} + H_{\text{Hubb}} + H_{so}$, where

$$H_{tb} = -\sum_{\langle i,j\rangle,s} (t_0 - \alpha\eta_{i,j}) C^{\dagger}_{i,s} C_{j,s} + \text{H.c.} \tag{1}$$

is the tight-binding contribution.

$$H_{\text{latt}} = \frac{1}{2}\sum_{\langle i,j\rangle} K(\eta_{i,j})^2 + \frac{1}{2}\sum_{i} \frac{P_i^2}{M} \tag{2}$$

describes each sublattice. It should be noted that our approach is a first-order approximation for the harmonic oscillator. As such, our approximation uses an effective K value that is parallel to the effective hopping term. Therefore, the K value employed differs from the one in Ref. [25], for we explicitly consider a single force constant as the Mo-S oscillator.

The electron-electron interactions are descried by the extended Hubbard model,

$$H_{ee} = U\sum_{i}\left(C^{\dagger}_{i,\uparrow}C_{i,\uparrow} - \frac{1}{2}\right)\left(C^{\dagger}_{i,\downarrow}C_{i,\downarrow} - \frac{1}{2}\right) + V\sum_{\langle i,j\rangle}(n_i - 1)(n_j - 1). \tag{3}$$

Finally, we describe the contribution of the spin-orbit interactions by

$$H_{so} = i\sum_{\langle j,l\rangle,s,s'} t_{so}\zeta_{j,l} C^{\dagger}_{j,s} s_z C_{l,s'}. \tag{4}$$

The main goal of the present work is to investigate the influence of the electron-phonon coupling constant on the system's behavior. In order to do so, we numerically simulate the system under a wide span of possible values of this parameter. The remaining constants were all extracted from the literature. It should be stressed that our model is general and can be parameterized to describe any TMDCN. However, in order to obtain comparable values, we decided to choose the remaining parameters to describe MoS_2 nanoribbons in particular. The parameters adopted here for the model Hamiltonian were $t_0 = 1.1$ eV [26], $K = 13.25$ eV/Å^2 [25], $a = 3.17$ Å [27], $U = 0.248$ eV, $V = 0.124$ eV [28], $t_{so} = 0.102$ eV [24], as well as the masses of molybdenum and sulfur. Such values were chosen in order to rescue the MoS_2 band gap and are consistent with the hopping and force constant parameters obtained in the literature [25,26].

Due to the nature of the system, two initial aspects are of special importance when it comes to the modeling of the charge distribution in TMDCN, the first being the influence of its size and the second being the value of the electron-phonon coupling parameter. As for the former, the influence of both the length and the width of the nanoribbons should be investigated because if polarons are to arise (in analogy to AGNRs), they might cover a large extension of the system, and an overlap between different parts of the same quasiparticle should be avoided. Preliminary investigations concerning the size of the system to be used should therefore be performed. The latter aspect is also critical for our purposes. Quasiparticles are known to result from the coupling between the degrees of freedom of the electronic and lattice parts of the system. Thus, since the actual value of the coupling parameter assumed by the model is a reflection of the conditions to which the system is subjected (as well as of its nature), a careful choice of α is central to our description.

In order to minimize edge effects, we chose to investigate the systems under periodic boundary conditions on the length of the nanoribbons. Following this procedure, we performed preliminary calculations (not shown here) by varying the length of the nanoribbons for different width sizes and for charged and uncharged nanoribbons. We chose the energy band gap of the system as the property of interest for the charge behavior description. Therefore, as criteria for determining the most suitable length of the systems, we have chosen the smallest possible nanoribbon from which a further size increase would not lead to a change in the band gap value keeping all the other parameters constant. These preliminary calculations resulted in nanoribbons 20 sites long. This length was kept constant during our analysis.

Besides length, the other fundamental geometric parameter is the width of the nanoribbon. Such a dimension is of particular importance because it determines the aforementioned confinement of the system's wave function. The narrow relation between electronic and structural aspects of the system is exploited in Fig. 1: we investigate the behavior of the energy gap as a function of different electron-phonon coupling values for different widths. Based on an analogy between the nanoribbons families described for AGNRs [29], we have also organized our results into different families, namely, $3p + 1$ in Fig. 1(a), $3p + 2$ in Fig. 1(b), and $3p$ in Fig. 1(c). Here, as originally, p is an integer that defines the rule of formation of each particular width. Figure 1(a) therefore presents widths of 4, 7, 10, 13, and 16 sites; Fig. 1(b) presents widths of 5,

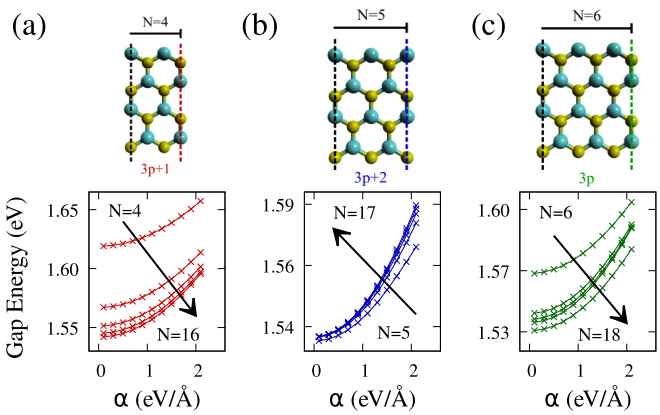

FIG. 1. Energy gap as a function of the electron-phonon coupling constant for the different families defined according to [29]. (a) The $3p+1$ family, (b) $3p+2$ family, and (c) $3p$ family. The diagram above each family is an example of the narrowest representative of that family. In it, the Mo sublattice is represented by the blue atoms (sublattice A), whereas S species are yellow (sublattice B).

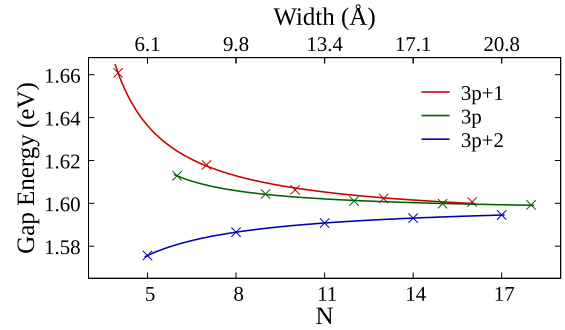

FIG. 2. Energy gap as a function of the nanoribbon width for the three families.

8, 11, 14, and 17 sites, and Fig. 1(c) presents widths of 6, 9, 12, 15, and 18 sites. Note that in the cases of families $3p+1$ [Fig. 1(a)] and $3p$ [Fig. 1(c)], higher widths correspond to smaller band gaps, as is the trend suggested by the smaller gaps in asymptotic sheets. Not only do the $3p+2$ nanoribbons, on the other hand, present the inverse behavior, but it is also clear that similar widths are associated with somewhat smaller band gaps when compared to their counterparts in other families of similar sizes. It should be noted that $3p+2$ is the same family that in AGNRs presents a quasimetallic behavior. Here, besides possessing a nonvanishing band gap even for narrow nanoribbons, one can see another very different behavior when compared to the other families: the dispersion among the curves that correspond to each width is much smaller, thus implying that, for this family, the width aspect is less important when compared to those of $3p$ and $3p+1$.

As a final important note one can see that, regardless of the particular nanoribbon studied, the dependence of the band gap on the electron-phonon constant is not larger than 0.05 eV. As the size of the nanoribbon can lead to influences twice as large, we can conclude that there exists a considerable range of possible electron-phonon coupling constants that correctly describes the system. As a matter of fact, no such thing as a "correct" value of α can be uniquely obtained, for different conditions to which the system is subjected should lead to slightly different band gaps. For instance, some theoretical results based on first-principles calculations have pointed to electron-phonon coupling values ranging in the interval 0.4–2.5 eV/A for pristine MoS_2 layers [30,31]. Rather, all one can think about is a correct range of values. Therefore, it makes sense to discuss the behavior of any particular electron-phonon coupling value within this correct range.

From the results of Fig. 1 and the experimental value of the band gap we can now explicitly discuss the dependence of the band gap on the length for a given α consistent with a reasonable range. This is important because, as previously mentioned, the band gap was observed to be much more dependent on the width than it was on the coupling constant. Figure 2 shows the dependence of the band gap on the nanoribbon width for the three families with $\alpha = 1.2$ eV/Å. Preliminary calculations have shown that the general trend remained consistent for other electron-phonon coupling values. One can readily see that in the $3p$ and $3p+1$ families the band gaps decrease as the width increases. As already mentioned, $3p+2$ family representatives show the opposite behavior while presenting a somewhat smaller gap value. The most interesting and useful feature of Fig. 2 is the asymptotic behavior suggested by the curves for large values of N. As the expected energy gap for transition metal dichalcogenides nanoribbons is around 1.6 eV [32], we can conclude that, indeed, the adopted electron-phonon coupling constant is accurate enough to use with our model since this was roughly the limiting value obtained for all the families. As an additional advantage, due to its asymptotic behavior, Fig. 2 also allows us to understand which nanoribbon size should be used if one desires to treat the system as a two-dimensional infinite sheet. Finally, because the considerable difference in the band gap should have consequences for the charge behavior, the results of Fig. 2 encouraged us to further discuss results related to charge distribution for both the broadest and narrowest nanoribbons. Up until this point, we have conducted a thorough investigation of all possible sizes between 4 and 18 sites and decided to show the results relative to these two limits. As the asymptotic behaviors of the three families for large N are similar, considering any of the largest nanoribbons of $3p$, $3p+1$, or $3p+2$ makes little difference. We take the broadest of them all, $N = 18$ for the $3p$ family. The behavior of narrow nanoribbons, on the other hand, is distinct. In this case, we simply chose to present the results of the smallest one, $N = 4$. This is a representative of the $3p+1$ family, so that by making this choice, we are showing results of the two comparable families, avoiding peculiarities of $3p+2$ that could introduce effects not necessarily caused by the width itself.

Using a α value consistent with the results from the band gap calculation and the width sizes determined from Fig. 2, we proceed to the investigation of the charged system. We simulate the extraction of one electron from the lattice, thus resulting in a positively charged carrier. Figures 3 and 4 summarize the main result of this work: we investigated the resulting charge carriers for different electron-phonon couplings for $N = 4$ and $N = 18$, respectively (a representative

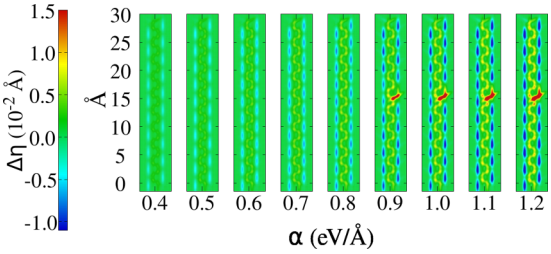

FIG. 3. Lattice distortion for several different electron-phonon (α) values in $N = 4$ TMDCN.

of the $3p + 2$ family, $N = 5$, is presented in Appendix B). The color pattern describes the charge distortion of the system, and each adjacent panel consists of a distinct electron-phonon coupling constant value. As the system is charged, it is the presence of the electron-phonon coupling that associates the lattice distortion with the accumulation of the net charge over the very region of the localized quasiparticle.

Figure 3 represents the narrowest nanoribbon, i.e., $N = 4$. For small electron-phonon coupling values, one can clearly see that the lattice distortion is evenly spread throughout the lattice length. This is consistent with the expected uncoupled degrees of freedom in the limiting case, in which the charge is rigorously indifferent to any geometrical property. As the electron-phonon constant value increases, a higher localized lattice distortion takes place. Although it is clear that a smooth localization process is in action, it is still possible to identify $\alpha = 0.9$ eV/Å (also observed by the inverse participation ratio shown in the Appendix B) as the critical electron-phonon coupling value in the sense that smaller couplings are associated with a somewhat dispersed distortion, whereas higher values yield lattice distortion typical of quasiparticles. As a matter of fact, a careful analysis of the distortion profile together with that of the charge density one (shown in Appendix B) allows one to conclude that quasiparticles such as polarons are also present in TMDCNs. This fact has profound consequences for the understanding of the transport mechanism as well as its properties, which are highly dependent on electron-electron and spin-orbit coupling, as shown in Appendix B. Importantly, scanning tunnel microscope topography and constant-current (dI/dV) maps can be used to study charge localization as performed in Ref. [33] for graphene nanoribbons. This might be a suitable experimental setup that could be employed to verify our results.

The lattice displacement of wider nanoribbons is presented in Fig. 4, which considers $N = 18$, for different electron-phonon constants. In this case, as the transition between localization regimes was observed to be much more abrupt, we decided to focus on only three values of α. In order to better analyze the details of the simulations, we included the nanoribbon in the top part of each panel with the associated projection of the distortion in the bottom. Figure 4(a) represents the $\alpha = 0.4$ eV/Å case, in which the charge is delocalized. The color pattern is clear in showing that, although a positive charge is included in the lattice, it responds with an evenly spaced distortion on the edges of the nanoribbons. Therefore, instead of creating a quasiparticle, this parametrization gave rise to only edge states, which are common features in TMDCNs [7]. Actually, by analyzing the projections, it can be noted that such edge states remain present in the system regardless of its coupling degree. The behavior of the system subjected to the critical electron-phonon value of $\alpha = 0.6$ eV/Å is depicted in Fig. 4(b). Note that, in this case, the evenly displaced distortion at the left edge of the figure has changed, giving place to a more pronounced distortion around its center, i.e., near 8 Å. By further increasing the coupling between the charge and lattice to $\alpha = 1.0$ eV/Å, we can see a very localized structure that gathers most of the extra charge included in the system around a few sites. This is the signature of a small polaron. We can therefore conclude that in studying the charge transport in TMDCNs, the quasiparticle picture should be taken into account. The polaron appears at a different edge and at a different site for each independent simulation. It is a spontaneous symmetry break induced in the self-consistent calculation by the excess of charge, as would happen to any polaron in other systems. For the sake of comparison, in Fig. 4 all nanoribbons have been translated or rotated by 180° for visually the same position. Such a presentation allows us to better compare the impact of the electron-phonon coupling on the lattice distortions.

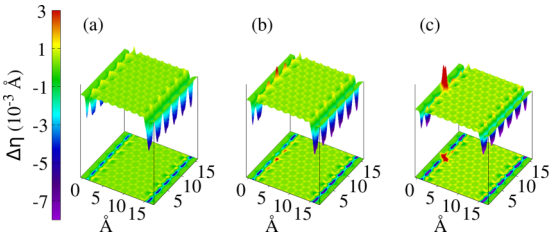

FIG. 4. Lattice distortion in $N = 18$ TMDCN for the electron-phonon constant (a) $\alpha = 0.4$, (b) 0.5, and (c) 0.6 eV/Å.

In summary, we developed an effective two-dimensional model to investigate the behavior of transition metal dichalcogenide nanoribbons. Such a model includes spin-orbit coupling, electron-electron interactions, and, most importantly, the coupling between the electronic and lattice parts of the system. As the latter parameter could be used to describe the system under different external conditions, we simulated the system subjected to a wide span of electron-phonon coupling values. We were able to obtain critical values of such a parameter that gives rise to either charge delocalization, or, alternatively, localized charge distortion. Besides edge states, which were observed to be present regardless of the coupling degree, we could see that for electron-phonon coupling constants higher than the critical value a quasiparticle with polaron characteristics arises. This aspect is fundamental because it shows that the quasiparticle picture ought to be considered when describing electronic transport in TMDCNs.

ACKNOWLEDGMENTS

The authors gratefully acknowledge the financial support from Brazilian research councils CNPq and the Brazilian Ministry of Planning, Development and Management Grant No. 005/2016 DIPLA. G.M.S., L.A.R.J., P.H.O.N., and W.F.C. also acknowledge the financial support from FAP-DF Grants No. 0193.001766/2017, No. 0193.001511/2017, No. 0193.001662/2017, and No. 0193.001694/2017, respectively.

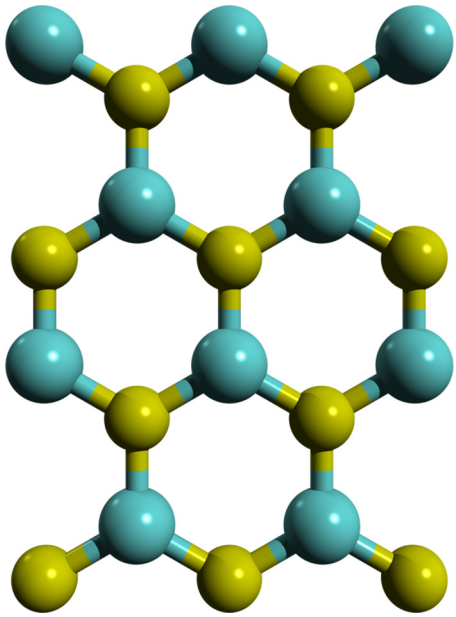

FIG. 5. Schematic structure of the TMDC nanoribbons. The yellow species represents the chalcogens, and the green atoms correspond to the transition metals.

APPENDIX A: METHODOLOGY

Our model describes transition metal dichalcogenides by considering an effective two-dimensional honeycomb lattice consisting of two sublattices (Fig. 5): one related to the chalcogens and the other to the transition metal. The model is completely general in the sense that the correct choice of its parameters allows one to describe different specific TMDC nanoribbons.

Figure 5 represents the simulated system. One can see that our model considers each metal atom directly linked to the chalcogen sites. The chalcogen sublattice is thus constructed in such a way to model the original system while maintaining the honeycomb structure of the model. This is accomplished by the determination of effective masses and elastic constants.

The system's electrons are quantumly treated within a second quantization approach, whereas the lattice is classically considered. These two realms are connected by means of the electron-phonon coupling term α, which includes lattice relaxation in the hopping integral of the system in a first-order expansion as follows:

$$t_{i,j} = t_0 - \alpha\eta_{i,j}. \tag{A1}$$

Here, t_0 is the hopping term adopted in conventional tight-binding models. Our model clearly goes beyond this approximation by making the electronic effects dependent on the lattice distortions, thus allowing for a more realistic behavior of the simulated system where $\eta_{i,j}$ is the variation of the bond distance between sites i and j.

The model Hamiltonian is composed of the following terms: H_{tb}, the tight-binding Hamiltonian with relaxation; H_{latt1} and H_{latt2}, each corresponding to either the metal or chalcogen sublattice; H_{Hubb}, which includes electronic correlation through extended Hubbard terms; and H_{so}, which includes the spin-orbit coupling.

The tight-binding part of the Hamiltonian is given by

$$H_{tb} = -\sum_{\langle i,j\rangle,s}(t_0 - \alpha\eta_{i,j})C^{\dagger}_{i,s}C_{j,s} + \text{H.c.} \tag{A2}$$

Here, $C_{i,s}$ is the annihilation operator of an s spin π electron in the ith site, and $C^{\dagger}_{j,s}$ is the corresponding creation operator in the jth site.

Each sublattice is classically treated in a harmonic approximation. By changing the suitable parameters, each one is described as

$$H_{\text{latt(1 or 2)}} = \frac{1}{2}\sum_{\langle i,j\rangle}K(\eta_{i,j})^2 + \frac{1}{2}\sum_i \frac{P_i^2}{M}. \tag{A3}$$

K is an effective Hooke-type elastic constant associated with the interatomic σ bonds considered in a harmonic approximation. P_i represents the momentum of each site, and M is its mass. The last term stands for the kinetic energy.

We include electron-electron interactions within an extended Hubbard formalism:

$$H_{ee} = U\sum_i\left(C^{\dagger}_{i,\uparrow}C_{i,\uparrow} - \frac{1}{2}\right)\left(C^{\dagger}_{i,\downarrow}C_{i,\downarrow} - \frac{1}{2}\right) + V\sum_{\langle i,j\rangle}(n_i - 1)(n_j - 1). \tag{A4}$$

In this expression $n_i = C^{\dagger}_{i,\uparrow}C_{i,\uparrow} + C^{\dagger}_{i,\downarrow}C_{i,\downarrow}$. U corresponds to the on-site electron-electron Coulombic interaction, and V is the neighboring-site electron-electron interactions.

Finally, the presence of the heavy metal species leads us to include the spin-orbit coupling:

$$H_{so} = i\sum_{\langle j,l\rangle,s,s'} t_{so}\zeta_{j,l}C^{\dagger}_{j,s}s_zC_{l,s'}. \tag{A5}$$

The l index spans all the next-nearest neighbor of atom j. $\zeta_{j,l}$ assumes a value of 1 for counterclockwise spin-orbit interaction and -1 for clockwise spin-orbit interaction provided j is in sublattice A. Conversely, if j pertains to B, the parameter is 1 for clockwise and -1 for the counterclockwise sense. s_z represents the Pauli matrix, and t_{so} is the spin-orbit hopping constant. In what follows, it is convenient to define the indices i' and i'': i' specifies the neighboring sites of site i, and i'' runs over the next-nearest-neighbor sites of i.

Considering the total Hamiltonian $H = H_{tb} + H_{\text{latt1}} + H_{\text{latt2}} + H_{ee} + H_{so}$, we carry out the calculations in a self-consistent way. Starting from an initial set of coordinates $\{\eta_{i,j}\}$ and given the values of t_0, K, α, t_{so}, U, and V, one can build a stationary electronic Hamiltonian. Performing a Hartree-Fock approximation for the electronic part of this total Hamiltonian leads us to the following eigenvalue problem, whose diagonalization provides the corresponding eigenvectors:

$$E_k\psi_{k,s}(i) = -\sum_{i'}[t_{i,i'} + V\tau_s(i,i')]\psi_{k,s}(i') + \left[U\left(\rho_{-s}(i) - \frac{1}{2}\right) + V\sum_{i'}\left(\sum_{s'}\rho_{s'}(i') - 1\right)\right] \times \psi_{k,s}(i) + \text{sgn}(s)\,it_{so}\sum_{i''}\zeta_{i,i''}\psi_{k,s}(i''), \tag{A6}$$

where

$$\rho_s(i) = \sum_k{}' \psi^*_{k,s}(i)\psi_{k,s}(i), \tag{A7}$$

$$\tau_s(i,i') = \sum_k{}' \psi^*_{k,s}(i)\psi_{k,s}(i'), \tag{A8}$$

and $\mathrm{sgn}(\uparrow) = +1$, $\mathrm{sgn}(\downarrow) = -1$. The prime means that sums are carried out only over occupied states.

With the eigenvectors we make the Slater determinant $|\Psi\rangle$ to evaluate expectation values. This is crucial here because the lattice is solved classically by means of the Euler-Lagrange equations. Therefore, in order to take lattice effects into account, one needs to obtain the expectation value of the system's Lagrangian, which is carried out using the wave function obtained through Eq. (A6) above and results in

$$\langle\Psi|L|\Psi\rangle = \frac{1}{2}\sum_{ij}\frac{P_{ij}^2}{M} - \frac{1}{2}\sum_{\langle i,j\rangle} K(\eta_{i,j})^2 + \sum_{\langle i,j\rangle,s}(t_0 - \alpha\eta_{ij})\langle\Psi|C^\dagger_{i,s}C_{j,s} + \mathrm{H.c.}|\Psi\rangle.$$

For the stationary solution,

$$\frac{\partial\langle\Psi|L|\Psi\rangle}{\partial\eta_{i,j}} = 0. \tag{A9}$$

This leads to

$$\eta_{i,j} = -\frac{\alpha}{K}\left[\sum_{k,s}{}' \psi^*_{k,s}(i)\psi_{k,s}(j) + \mathrm{c.c.}\right]. \tag{A10}$$

It should be noted that the electronic and lattice parts of the system are coupled by Eqs. (A6) and (A10).

One can finally solve the Euler-Lagrange equation for the stationary case to obtain η_{ij} to be used in the self-consistent procedure. A solution, self-consistent for the degrees of freedom of both electrons and the lattice, is obtained by considering a set $\{\eta_{i,j}\}$, calculating the corresponding set $\{\psi_{k,i}\}$, and solving to obtain new values $\{\eta_{i,j}\}$ until convergence is achieved.

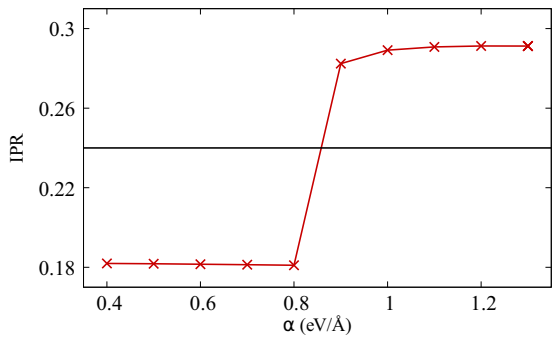

FIG. 6. Inverse participation ratio (IPR) as a function of the electron-phonon coupling constant α. The dashed line represents a critical value of IPR. Above it a polaron is present in the system.

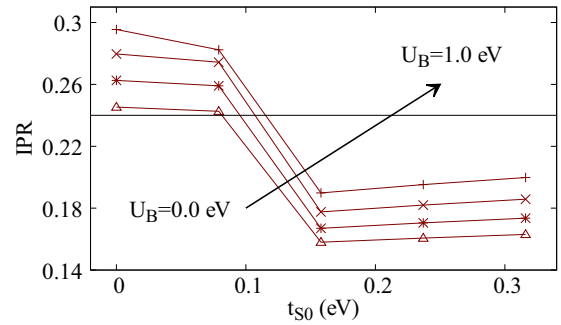

FIG. 7. IPR as a function of the spin-orbit coupling parameter t_{so} for several electron-correlation degrees expressed by the Hubbard constant U_B: 0, 0.5, 0.75, and 1.00 eV. The arrow shows the direction of increasing electron-electron interaction.

APPENDIX B: SUPPLEMENTARY DATA

We use the inverse participation ratio (IPR) as a tool to quantify the formation of a quasiparticle. Indeed, such a quantity is a measurement of the charge localization degree in the system and is defined as

$$\mathrm{IPR} = \frac{\sum_{i,s}|\rho_s(i)|^4}{(\sum_{i,s}|\rho_s(i)|^2)^2}. \tag{B1}$$

From Fig. 6 we observe a critical IPR value of 0.24, above which the described system presents polarons and, correspondingly, below which the charge is considered to be delocalized. These results are relative to $N = 4$, but other widths presented qualitatively similar results. Figure 6 represents the localization pattern as a function of the electron-phonon coupling constant. One can see that the critical value of α is 0.9 eV/Å. This means that simulations that considered values higher than this one typically yielded a polaron. Values of 0.8 and lower corresponded to the delocalization of the charge. This corresponds to a phase transition in the behavior of the charge distribution in TMDCNs, as suggested by Fig. 6.

Figure 7 corresponds to the dependence of IPR on the spin-orbit coupling term for different sets of electron-electron correlations. This calculation was also performed for $N = 4$, and again, different widths presented similar behavior, albeit with quantitative differences. A general trend that can be observed is that typically an increase in spin-orbit coupling causes a decrease in the charge localization degree.

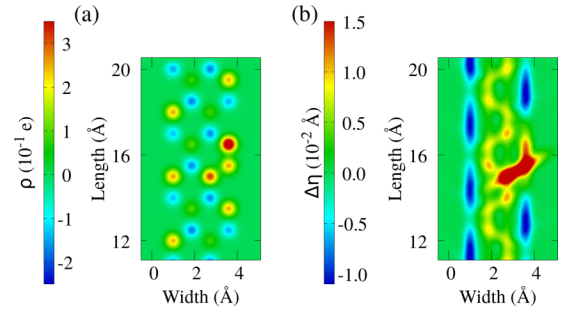

FIG. 8. (a) Charge density and (b) lattice distortion associated with a polaron in a transition metal dichalcogenide nanoribbon with width $N = 4$.

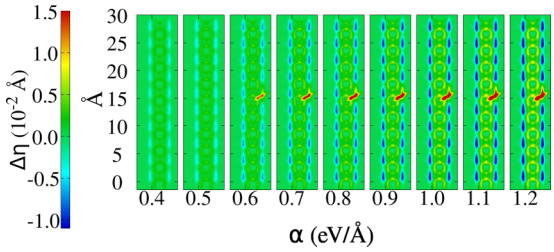

FIG. 9. Lattice distortion for several different electron-phonon constant α values in $N = 5$ nanoribbon, i.e., a representative of the $3p + 2$ family of TMDCN.

A spin-orbit parameter greater than 0.15 resulted in charge delocalization regardless of the electron correlation values. Another interesting feature is that increasing electron-electron interaction acted towards increasing the localization of the system, favoring the formation of polarons.

Figure 8(a) presents a zoom of the charge density profile corresponding to the simulation shown in Fig. 3 of the main text [also zoomed here is the corresponding lattice distortion in Fig. 8(b)]. The extra positive charge is concentrated in the edges, while some negative charge is spread mainly through the middle. The polaron is localized in this edge, as can be seen by both charge localization and lattice deformation around the same region. One can see that, although the same information is conveyed by both panels, in the charge density profile it is considerably more difficult to visualize than in the lattice displacement.

Figure 9 shows the charge localization behavior of a TMDC nanoribbon with a width of 5 sites, i.e., of the $3p + 2$ family, for different α values. One can see that the overall behavior is remarkably similar to the one shown in Fig. 3 of the main text. Different families present different quantitative properties while preserving the same trend.

[1] K. Kim, J. Y. Choi, S. H. C. T. Kim, and H. J. Chun, Nature (London) **479**, 338 (2011).
[2] X. Pan, W. Qiu, and E. Skafidas, Sci. Rep. **6**, 36167 (2016).
[3] A. Kumar and P. K. Ahluwalia, Eur. Phys. J. B **85**, 186 (2012).
[4] J. Wilson and A. Yoffe, Adv. Phys. **18**, 193 (1969).
[5] E. C. A. Ayari, O. Ogundadegbe, and M. S. Fuhrer, J. Appl. Phys. **101**, 014507 (2007).
[6] S. Manzeli, D. Ovchinnikov, D. Pasquier, O. V. Yazyev, and A. Kis, Nat. Rev. Mater. **2**, 17033 (2017).
[7] Qing Hua Wang, Kourosh Kalantar-Zadeh, Andras Kis, Jonathan N. Coleman, and Michael S. Strano, Nat. Nanotechnol. **7**, 699 (2012).
[8] B. Sipos, A. F. Kusmartseva, A. Akrap, H. Berger, L. Forró, and E. Tutiš, Nat. Mater. **7**, 960 (2008).
[9] J. Wilson, F. D. Salvo, and S. Mahajan, Adv. Phys. **24**, 117 (1975).
[10] A. H. Castro Neto, Phys. Rev. Lett. **86**, 4382 (2001).
[11] M. Trushin, M. O. Goerbig, and W. Belzig, Phys. Rev. Lett. **120**, 187401 (2018).
[12] G. Moody, K. Tran, X. Lu, T. Autry, J. M. Fraser, R. P. Mirin, L. Yang, X. Li, and K. L. Silverman, Phys. Rev. Lett. **121**, 057403 (2018).
[13] A. Politano, G. Chiarello, B. Ghosh, K. Sadhukhan, C.-N. Kuo, C. S. Lue, V. Pellegrini, and A. Agarwal, Phys. Rev. Lett. **121**, 086804 (2018).
[14] W. F. da Cunha, L. A. Ribeiro Junior, R. Gargano, and G. M. e Silva, Phys. Chem. Chem. Phys. **16**, 17072 (2014).
[15] W. F. da Cunha, L. A. R. Junior, A. L. de Almeida Fonseca, R. Gargano, and G. M. e Silva, Carbon **91**, 171 (2015).
[16] W. Wang, C. Yang, L. Bai, M. Li, and W. Li, Nanomaterials **8**, 74 (2018).
[17] S. Hu, M. Lozada-Hidalgo, F. C. Wang, A. Mishchenko, F. Schedin, R. R. Nair, E. W. Hill, D. W. Boukhvalov, M. I. Katsnelson, R. A. W. Dryfe, I. V. Grigorieva, H. A. Wu, and A. K. Geim, Nature (London) **516**, 227 (2014).
[18] G. M. e Silva, Phys. Rev. B **61**, 10777 (2000).
[19] P. H. de Oliveira Neto, J. F. Teixeira, W. F. da Cunha, R. Gargano, and G. M. e Silva, J. Phys. Chem. Lett. **3**, 3039 (2012).
[20] W. P. Su, J. R. Schrieffer, and A. J. Heeger, Phys. Rev. Lett. **42**, 1698 (1979).
[21] W. P. Su, J. R. Schrieffer, and A. J. Heeger, Phys. Rev. B **22**, 2099 (1980).
[22] W. Ferreira da Cunha, P. H. de Oliveira Neto, A. Terai, and G. Magela e Silva, Phys. Rev. B **94**, 014301 (2016).
[23] P. H. de Oliveira Neto and T. V. Voorhis, Carbon **132**, 352 (2018).
[24] S. Konschuh, M. Gmitra, and J. Fabian, Phys. Rev. B **82**, 245412 (2010).
[25] A. Molina-Sánchez and L. Wirtz, Phys. Rev. B **84**, 155413 (2011).
[26] D. Xiao, G.-B. Liu, W. Feng, X. Xu, and W. Yao, Phys. Rev. Lett. **108**, 196802 (2012).
[27] F. Zahid, L. Liu, Y. Zhu, J. Wang, and H. Guo, AIP Adv. **3**, 052111 (2013).
[28] E. Cappelluti, R. Roldán, J. A. Silva-Guillén, P. Ordejón, and F. Guinea, Phys. Rev. B **88**, 075409 (2013).
[29] L. Yang, C.-H. Park, Y.-W. Son, M. L. Cohen, and S. G. Louie, Phys. Rev. Lett. **99**, 186801 (2007).
[30] T. Gunst, T. Markussen, K. Stokbro, and M. Brandbyge, Phys. Rev. B **93**, 035414 (2016).
[31] K. Kaasbjerg, K. S. Thygesen, and K. W. Jacobsen, Phys. Rev. B **85**, 115317 (2012).
[32] S.-L. Xiao, W.-Z. Yu, and S.-P. Gao, Surf. Sci. **653**, 107 (2016).
[33] D. J. Rizzo, G. Veber, T. Cao, C. Bronner, F. Z. Ting Chen, H. Rodriguez, S. G. Louie, M. F. Crommie, and F. R. Fischer, Nature (London) **560**, 204 (2018).